

1 Article

2 

# Numerical model for predicting bead geometry and

  
3 

# microstructure in Laser Beam Welding of Inconel 718

  
4 

# sheets

5 **Iñigo Hernando** <sup>1,\*</sup>, **Jon Iñaki Arrizubieta** <sup>1</sup>, **Aitzol Lamikiz** <sup>1</sup> and **Eneko Ukar** <sup>1</sup>6 <sup>1</sup> University of the Basque Country (UPV/EHU), Dpt. Of Mechanical Engineering - EIB Bilbao, Plaza Torres  
7 Quevedo 1, Bilbao, 48013, Spain.8 \* Correspondence: [inigo.hernando@ehu.eus](mailto:inigo.hernando@ehu.eus); Tel.: +34-946-017-347

9

10 **Abstract:** A numerical model was developed for predicting the bead geometry and microstructure  
11 in Laser Beam Welding of 2 mm thickness Inconel 718 sheets. The experiments were carried out  
12 with a 1 kW maximum power fiber laser coupled with a galvanometric scanner. Wobble strategy  
13 was employed for sweeping 1 mm wide circular areas for creating the weld seams and a specific  
14 tooling was manufactured for supplying protective Argon gas during the welding process. The  
15 numerical model takes into account both the laser beam absorption and the melt-pool fluid  
16 movement along the bead section, resulting in a weld geometry that depends on the process input  
17 parameters, such as feed rate and laser power. The microstructure of the beads was also estimated  
18 based on the cooling rate of the material. Features as bead upper and bottom final shapes, weld  
19 penetration and dendritic arm spacing were numerically and experimentally analyzed and  
20 discussed. The results given by the numerical analysis agree with the tests, making the model a  
21 robust predictive tool.22 **Keywords:** laser; welding; LBW; model; microstructure; bead seam; wobble strategy; Inconel 718.  
2324 

## 1. Introduction

25 The Laser Beam Welding (LBW) is a material joining technique that apply a laser radiation to  
26 melt the base material and create the welding joint. LBW process is related to other traditional  
27 welding methods such as Electron Beam Welding (EBW), Tungsten Plasma Arc Welding (PAW) or  
28 Inert Gas Tungsten Arc Welding (TIG). LBW apply a high power industrial laser to create a narrow  
29 and deep melt pool between the parts to be welded. Laser is a highly concentrated heat source that  
30 can be easily automated and installed on industrial welding cells, providing high welding speeds for  
31 many industrial applications. Nevertheless, factors such as the laser beam quality or the processed  
32 materials have a great influence on the resulting geometry, microstructure and residual stress  
33 distribution. Therefore, final results are directly dependent on the process input parameters [1], what  
34 means that process parameters must be carefully selected for achieving the desired quality [2].35 LBW modeling represents a basic tool for predicting the temperature field and giving accurate  
36 information about shape of the melt pool and final shape of the bead depending on the process  
37 parameters (welding speed, laser power, workpiece geometry, etc.). This fact has a direct impact on  
38 reducing the costs derived from experimental tests [3].39 Modern aircraft engines require materials capable of withstanding high temperatures without  
40 lowering their mechanical properties. In order to fulfil this task, nickel-based alloys comprise about  
41 50% of the total weight of the engines used in aerospace industry, providing high temperature  
42 strength and good resistance against wear or corrosion thanks to their chemical stability [4].  
43 Aeronautical structures design and fabrication search for minimum weight models that may put up  
44 with several flight work conditions. Since Ni alloys machinability is relatively low and the cost of the  
45 material is high, welding techniques present high advantages over machining. On the one hand,

46 welding can be used for building complex structures from smaller parts and, on the other hand,  
47 wasted material and chip formation is drastically reduced.

48 Inconel 718 superalloy is widely used in gas turbine components as Tail Bearing Housings  
49 (TBH), which have to deal with high temperature gradients and corrosive environments. The strength  
50 of the material comes mainly from small  $\gamma'$  and  $\gamma''$  precipitates that are high in Ni content [5]. On the  
51 other hand, despite the Inconel 718 alloy has a reasonably good resistance against weld solidification  
52 cracking, it is slightly prone to the appearance of microfissures in the HAZ [6], so LBW is an  
53 appropriate joining method as it affects just a narrow zone.

54 Regarding this fact, modeling and study is needed in order to check weld integrity, as LBW is  
55 an innovative assembling method both for dispensing rivets and for its good qualities compared to  
56 other conventional welding techniques [7]. Besides, LBW has arisen as an alternative to Electron  
57 Beam Welding (EBW), which can only be used in a vacuum chamber and requires a more complex  
58 fixturing, what results in a much more expensive process.

59 In terms of pores formation, nickel-based alloys with chromium (as Inconel 718) are susceptible  
60 to this phenomenon during the welding process, having to resort to protective gases in order to avoid  
61 pores [8].

62 The laser power level that material absorbs can be reasonably predicted, so the effects of the heat  
63 input may be accurately estimated by a numerical model [9]. The absorptivity of the material  
64 represents the ratio of the energy that the workpiece absorbs, it is one of the basis for any heat transfer  
65 calculation [10] and hence, modeling must consider this characteristic for any reliable result.  
66 Moreover, other effects need to be considered in laser welding processes such as convective and  
67 thermocapillary forces that cause deformations during the solidification after the melting phase.  
68 These forces are generated due to a decrease of the surface tension of the molten material as  
69 temperature increases, which leads to material flow between hot and cold regions [11]. This  
70 phenomenon, named as Marangoni effect, has a direct impact on the weld bead geometry [12].  
71 Therefore, the model must consider this effect in order to achieve the desired accuracy and predict  
72 the welding profile.

73 At the beginning of the LBW technology, Swift-Hook and Gick stated that lasers opened a wide  
74 range of possibilities according to deep welds [13] and Klemens declared the many factors as heat,  
75 vapor flow, gravity or surface tension are directly connected with the final shape of the seam.  
76 Moreover, the need of experimental tests for validating the theoretical heat models took force for  
77 identifying unknown factors [14].

78 In the 80s, Mazumder praised the importance of better understanding of the melt pool  
79 generation and fluid flow in order to improve the potential of the mathematical models, making them  
80 predictive powerful tools [10]. In the same way, Goldak et al. asserted that the prediction of aspects  
81 such as the strength of the welded structures, which is directly related to residual stress or distortions,  
82 called for precise analysis of the thermal cycles for further modeling [15].

83 Afterwards, Bonollo et al. assured that the laser welding dynamics were not entirely understood,  
84 despite theoretical evaluation and subsequent experimental validation had enabled to develop the  
85 comprehension of the LBW technique [16]. This statement was confirmed by Kaplan et al., who  
86 placed value on modeling for improving the physical understanding of the LBW process [17].  
87 Ducharme et al., for their part, stood out that modeling allowed to demonstrate the relation between  
88 the keyhole and the melt pool [18].

89 Sudnik et al. alleged the need of new theoretical work in order to better the laser welding process  
90 as well as its control and defects description. This was grounded on the fact that many heat  
91 conduction models did not achieve the desired accuracy when predicting the weld bead geometry  
92 [19]. Nevertheless, Tsirkas et al. pointed the difficulty of modeling the welding process, as thermal,  
93 mechanical and metallurgical phenomena take place at the same time [20]. Furthermore, Gery et al.  
94 concluded that the experimental work is mandatory for determining relations between heat source  
95 models and subsequent empirical testing [21].

96 Later, Kazemi and Goldak continued maintaining the idea that modeling the laser keyhole  
97 welding was still challenging and defended the idea of simplifying the models for describing the

98 temperature fields [3]. In turn, Zhao et al. affirmed that the coexistence of three different phases  
 99 (plasma, liquid and solid) added to the complex keyhole behavior and the forces acting in the weld  
 100 pool made modeling still difficult [22].

101 Likewise, Kubiak et al. underlined the necessity of an innovative focusing on the theory and  
 102 numerical solution techniques used for the LBW, as this process offers characteristic heat  
 103 distributions compared to traditional welding methods [23]. However, Zhang et al. pointed that  
 104 despite of the advances in laser deep penetration knowledge due to numerical simulation, yet many  
 105 issues remain unexplored [24].

106 For this reason, it is concluded that there is a need in the aerospace industry to develop a model  
 107 that predicts the geometry of the resulting joint when welding thin Inconel 718 plates. Therefore, a  
 108 model that considers the melt pool dynamics during the welding process is developed. In addition,  
 109 the obtained results have been experimentally validated under different conditions. Moreover, the  
 110 numeric tool is capable of predicting the generated microstructure based on the thermal field  
 111 variations during the process.

112 **Table 1.** Employed symbols and nomenclature.

Symbol	Description	Unit
$u$	Fluid velocity in the X axis direction.	$\text{m}\cdot\text{s}^{-1}$
$v$	Fluid velocity in the Y axis direction.	$\text{m}\cdot\text{s}^{-1}$
$U$	Absolute fluid velocity.	$\text{m}\cdot\text{s}^{-1}$
$\Delta x$	Element size in the X axis direction.	$\text{m}$
$\Delta y$	Element size in the Y axis direction.	$\text{m}$
$\rho$	Material density.	$\text{kg}\cdot\text{m}^{-3}$
$p$	Pressure value.	$\text{N}\cdot\text{m}^{-2}$
$\mu$	Material viscosity.	$\text{kg}\cdot\text{m}^{-1}\cdot\text{s}^{-1}$
$g$	Gravitational acceleration constant.	$\text{m}\cdot\text{s}^{-2}$
$\hat{e}$	$Y+$ direction unitary vector.	-
$\gamma$	Volume fraction (solid/liquid).	-
$f_s$	Surface forces.	$\text{N}$
$\sigma$	Surface tension.	$\text{N}\cdot\text{m}^{-1}$
$\frac{d\sigma}{dT}$	Surface tension variation regarding the temperature.	$\text{N}\cdot\text{m}^{-1}\cdot\text{K}^{-1}$
$\kappa$	Surface curvature.	$\text{m}^{-1}$
$\vec{n}$	Vector normal to the surface (solid/liquid – gas interface).	-
$\beta$	Coefficient of liquid thermal expansion.	$\text{K}^{-1}$
$c$	Specific energy.	$\text{J}\cdot\text{kg}^{-1}\cdot\text{c}$
$k$	Heat conductivity.	$\text{W}\cdot\text{m}^{-1}\cdot\text{K}^{-1}$
$S_L$	Fusion latent heat.	$\text{J}\cdot\text{kg}^{-1}$
$T$	Temperature.	$\text{K}$
$T_S$	Solidus temperature.	$\text{K}$
$T_L$	Liquidus temperature.	$\text{K}$
$T_\infty$	Room temperature.	$\text{K}$
$t$	Time variable.	$\text{s}$
$\Delta t$	Time step.	$\text{s}$
$P$	Laser power.	$\text{W}$
$q_{laser}$	Laser beam intensity.	$\text{W}\cdot\text{m}^{-2}$
$q_{losses}$	Energy losses due to radiation and convection.	$\text{W}\cdot\text{m}^{-2}$
$r_{out}$	Outer radius of the laser beam in the wobble strategy.	$\text{m}$
$r_{in}$	Inner radius of the laser beam in the wobble strategy.	$\text{m}$
$\alpha$	Absorptivity.	-
$h$	Convection coefficient.	$\text{W}\cdot\text{m}^{-2}\text{K}^{-1}$
$\varepsilon$	Emissivity.	-

$\sigma_b$	Stefan-Boltzmann coefficient.	$\text{W} \cdot \text{m}^{-2} \text{K}^{-4}$
$\delta$	Angle between the laser beam and the normal vector to the surface	rad
$v_f$	Welding feed rate.	$\text{mm} \cdot \text{s}^{-1}$
$v_p$	Peripheral speed in the wobble operation	$\text{mm} \cdot \text{s}^{-1}$

113

114 **2. Developed model**115 *2.1 Model Basis*

116 The proposed model is based on solving the continuity (1), momentum (2) and energy  
 117 conservation (3) equations in order to obtain the pressure, velocity and temperature fields of each  
 118 element respectively. The coupled pressure-velocity equations are solved using the SIMPLE  
 119 algorithm proposed by Patankar [25] and a fully implicit scheme is used.  
 120

$$\frac{\partial \rho}{\partial t} + \frac{\partial}{\partial x}(\rho \cdot u) + \frac{\partial}{\partial y}(\rho \cdot v) = 0 \quad (1)$$

$$\frac{\partial}{\partial t}(\rho \cdot \phi) + \frac{\partial}{\partial x}(\rho \cdot u \cdot \phi) + \frac{\partial}{\partial y}(\rho \cdot v \cdot \phi) = -\frac{\partial p}{\partial x} + \frac{\partial}{\partial x}\left(\mu \cdot \frac{\partial \phi}{\partial x}\right) - \frac{\partial p}{\partial y} + \frac{\partial}{\partial y}\left(\mu \cdot \frac{\partial \phi}{\partial y}\right) + S_m \quad (2)$$

$$\frac{\partial}{\partial t}(\rho \cdot c \cdot T) + \frac{\partial}{\partial x}(\rho \cdot c \cdot u \cdot T) + \frac{\partial}{\partial y}(\rho \cdot c \cdot v \cdot T) = \frac{\partial}{\partial x}\left(k \cdot \frac{\partial T}{\partial x}\right) + \frac{\partial}{\partial y}\left(k \cdot \frac{\partial T}{\partial y}\right) + S_e \quad (3)$$

121

122 The momentum generation term ( $S_m$ ) includes the buoyancy force ( $S_b$ ) generated as a  
 123 consequence of the density difference and the velocity reduction term ( $S_d$ ) introduced in those  
 124 elements where the material is in solid state. Material is considered completely rigid and  
 125 incompressible when it is in solid state, therefore, the velocity of the material in the solid region is  
 126 zero. This is modeled by the second term in equation (4), where the parameter  $f_l$  has a zero value in  
 127 the solid and a unit value in the liquid. In order to avoid zeros in the denominator,  $C=10^6$  and  $e_0=10^{-3}$   
 128 values are adopted [25].  
 129

$$S_m = S_b + S_d = \rho \cdot g \cdot \beta \cdot (T - T_\infty) \cdot \vec{e} - \frac{C \cdot (1 - f_l)}{f_l^3 + e_0} \cdot U \quad (4)$$

130

131 Regarding the energy generation term ( $S_e$ ), equation (5), includes the latent heat ( $S_L$ ) and the heat  
 132 exchange at the substrate surface ( $S_C$ ). Inside this second term, the energy radiated by the laser beam  
 133 ( $q_{laser}$ ) and the heat losses due to radiation and convection ( $q_{losses}$ ) are included. As no material  
 134 vaporization is expected, the model includes only the fusion latent heat, which is defined in equation  
 135 (6).  
 136

$$S_e = S_L + S_C = S_L + q_{laser} - q_{losses} \quad (5)$$

$$S_L = \rho \cdot \frac{\partial L}{\partial t} = \rho \cdot \frac{\partial L}{\partial T} \cdot \frac{\partial T}{\partial t} \quad (6)$$

137

138 The energy input at the surface can be approximated as a ring-type source, generated by a fast-  
 139 moving laser spot that follows a wobble strategy, as it is shown in Figure 1. Therefore, the energy  
 140 input in a surface element located at an  $x$  and  $y$  planar distance from the laser beam center point is  
 141 defined by means of equation (7). As the free surface can deform freely, the absorptivity value ( $\alpha$ ) is  
 142 modified as a function of the angle between the laser beam centerline and the normal vector to the

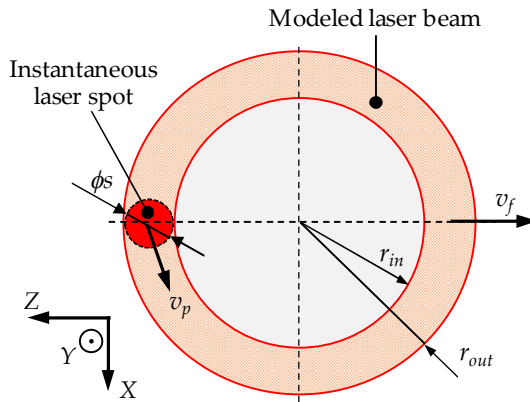
143 free surface ( $\delta$ ). On the other hand, radiation and convection losses at the surface of the substrate are  
 144 described by equation (8), where  $n$  is the number of free-faces of a certain element located on the  
 145 surface.

146

$$q_{laser} = \frac{2 \cdot \alpha \cdot \cos(\delta) \cdot P}{\pi \cdot (r_{out}^2 - r_{in}^2)} \quad (7)$$

$$q_{losses} = n \cdot [h \cdot (T - T_{\infty}) + \varepsilon \cdot \sigma_b \cdot (T^4 - T_{\infty}^4)] \quad (8)$$

147



148

149

150 **Figure 1.** Instantaneous laser spot and modeled laser beam in wobble strategy

151

152 The model considers conduction and diffusion as heat transfer mechanisms within the material.  
 153 Moreover, the Volume of Fluid (VOF) equation (9) is solved to determine the material movement and  
 154 the variation of the free surface. For tracking the interface, the interface capturing method is used  
 155 because, unlike other methods, does not introduce restrictions to the evolution of the free surface.  
 156 This method gives the position of the boundary between the different phases by using a scalar  
 157 transport variable. The volume fraction ( $\gamma$ ) becomes a zero value in the gas and a unit value in the  
 158 base material (solid or liquid). So, the interface is defined as the transition zone where  $\gamma$  takes a value  
 159 between zero and the unit.

160

$$\frac{\partial \gamma}{\partial t} + \nabla(\gamma \cdot U) = 0 \quad (9)$$

161

162 The residue value to ensure the convergence of the results is set to a  $10^{-3}$  value between two  
 163 subsequent iterations [25]. The same criteria is used for mass, momentum, energy conservation and  
 164 VOF equations.

## 165 2.2 Initial and boundary conditions

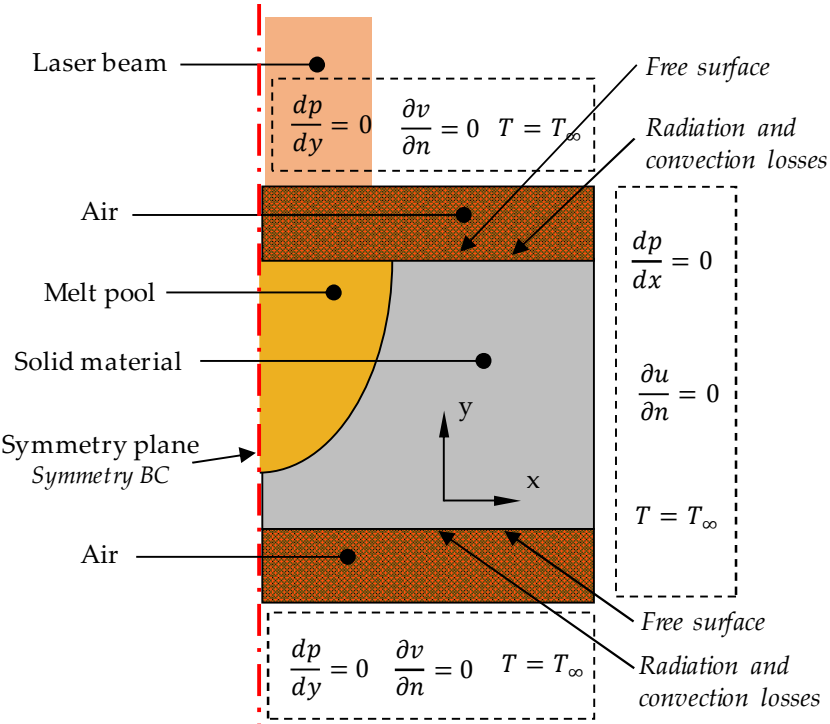
166 In order to start the simulation, the initial temperature of all elements must be defined. since no  
 167 preheating stage has been considered, all nodes are supposed to be at room temperature ( $T_{\infty}=298$  K).  
 168 Therefore, the whole substrate is in solid state at the initial stage and all the elements have a  
 169 zero-velocity value.

170 Velocity, pressure and temperature values are determined at the limits of the model by means  
 171 of the boundary conditions, see Figure 2. On the one hand, a zero-pressure gradient condition is  
 172 established in all the boundaries. On the other hand, a zero-velocity vector variation condition is  
 173 established in all boundary faces. Lastly, in terms of temperature boundaries, the nodes next to the  
 174 control volume are forced to be at room temperature ( $T_{\infty}=298$  K). This is equivalent to consider a first  
 175 specie or Dirichlet boundary condition, equation (10).

176

$$q = k \cdot \left( \frac{\partial T}{\partial x} + \frac{\partial T}{\partial y} \right) \quad (10)$$

177



178

**Figure 2.** Applied boundary conditions for modeling the welding process.

179

180

With the aim of reducing unnecessary computational cost and based on the symmetric nature of the modeled problem, just half of the volume is simulated. The following boundary conditions are set in the symmetry plane:

181

$$\frac{dT}{dy} = 0 \quad ; \quad u = 0 \quad ; \quad \frac{dv}{dx} = 0 \quad (11)$$

182

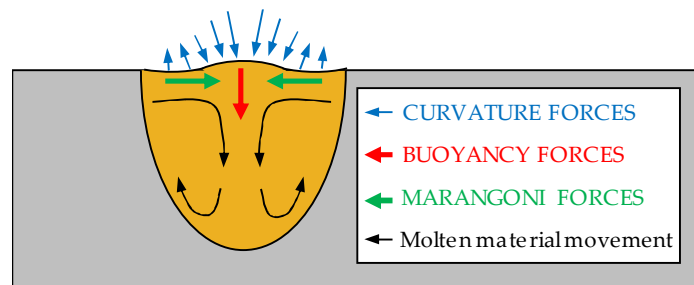
### 2.3 Surface forces

183

Movement of the molten material is generated due to surface forces, see equation (12). On the one hand, a force normal to the surface takes place due to the curvature developed by the interface between the air and substrate. On the other hand, Marangoni forces are generated because of the surface stress variation regarding the temperature variation. Besides, buoyancy forces are included in the model, which generate a downwards force. All forces considered in the model are shown in Figure 3.

184

$$f_s = \left[ \sigma \cdot \kappa \cdot \vec{n} + \frac{d\sigma}{dT} [\nabla T - \vec{n} \cdot (\vec{n} \cdot \nabla T)] \right] \quad (12)$$

193  
194  
195**Figure 3.** Material movement due to the surface and buoyancy forces.196 **2.4 Microstructure**

197 The internal structure of material after melting and solidifying depends directly on the process  
 198 cooling rate. When the temperature drops below the liquidus temperature ( $T_L$ ), columnar dendritic  
 199 microstructure is formed until the solidus temperature ( $T_s$ ) is reached. This temperature phase-  
 200 change range is named as the mushy zone [26].

201 The interplanar spacing between different dendrites can be estimated based on the cooling rate  
 202 and the boundary temperatures where the material undergoes the phase changes, which are the  $T_L$   
 203 and the  $\gamma$ /laves eutectic temperature ( $T_e$ ). At this juncture, dendritic columns grow mainly in the  
 204 energetically favorable crystallographic directions, forming the principal axis and, to a lesser extent,  
 205 in the other transverse secondary directions [6]. The secondary dendrite arm spacing (SDAS) is  
 206 measured in this research tests for subsequent thermal model validation by means of equation (13).  
 207 To this end, the mean values are calculated based on ten different measurements for each analyzed  
 208 welding bead. SDAS is measured in  $\mu\text{m}$  and  $C$  is a constant that depends on the material. For the  
 209 specific case of the Inconel 718 this constant takes a value of 10 [27].  
 210

$$SDAS = C \cdot \left( \frac{T_L - T_e}{\frac{dT}{dt}} \right)^{1/3} \quad (13)$$

211  
212  
213  
214  
215

The Inconel 718 is a widely used and studied material and therefore, many authors have contributed with their research to the determination of these reaction temperatures. In the present investigation, the values given by Eiselstein for the cooling case are considered [28]: 1260 °C and 1177 °C for the liquidus temperature ( $T_L$ ) and the  $\gamma$ /laves eutectic temperature ( $T_e$ ), respectively.

216 **Table 2.** Inconel 718 cooling temperatures.

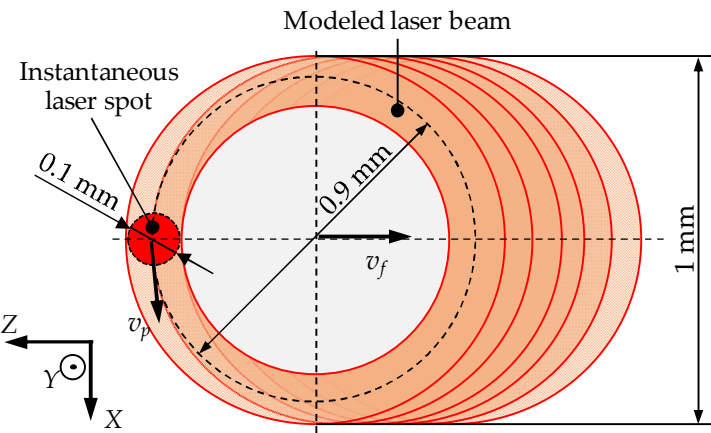
Reaction stage	Value (°C)
Liquidus on cooling	1260
Solidus on cooling	1227
$\gamma$ /laves eutectic on cooling	1177

217

218 **3. Proposed methodology for the model validation**

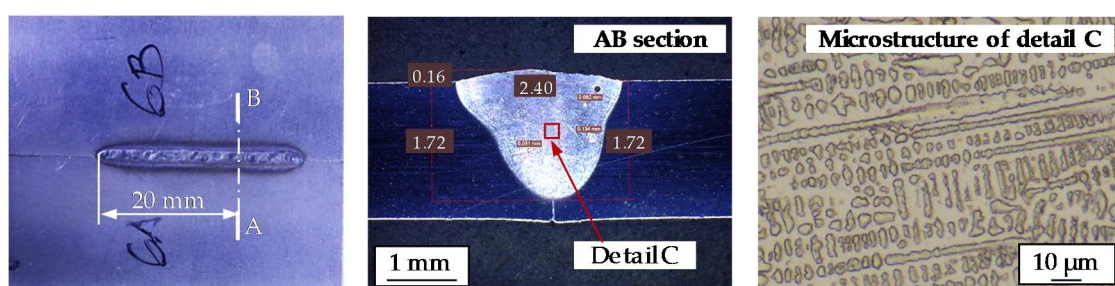
219 Validation has been carried out using FL010 1kW fiber laser from Rofin FL010 with an output  
 220 fiber of 100  $\mu\text{m}$  coupled to galvanometric scan head hurrySCAN® 25 from SCANLAB with a  
 221 maximum workspace of 120 x 120 mm and maximum feed rate of 10,000  $\text{mm} \cdot \text{s}^{-1}$ . Scan head allows  
 222 fast movements of the laser beam because of the low inertia of the moving mirrors, giving as result  
 223 high velocities and accelerations without losing positioning accuracy. Therefore, the laser beam  
 224 motion is fast enough to consider as a ring-type spot of 1 mm diameter that moves at a  $v_f$  feed rate

225 speed. In this case, a wobble strategy is used for the welding process, see Figure 4. This method allows  
 226 to fill an area by describing rings, so a suitable relation between the feed rate ( $v_f$ ) and the peripheral  
 227 speed ( $v_p$ ) is implemented for achieving minimum overlap and no space among consecutive rings.  
 228 So, the laser spot must spend the same time for tracing a loop (orbital motion) and for advancing a  
 229 spot diameter distance (linear movement).



230  
 231 **Figure 4.** Wobble scanning technique employed for the welding operation  
 232

233 The selected continuous laser powers for welding the 2 mm thickness Inconel 718 sheets are  
 234 350 W, 400 W, 450 W and 500 W in combination with two different feed rates: 3  $\text{mm}\cdot\text{s}^{-1}$  and 5  $\text{mm}\cdot\text{s}^{-1}$ .  
 235 The seam length is of 30 mm, enough to ensure steady state is achieved during welding track.  
 236 Afterwards, all the samples are cut at a 20 mm distance from the beginning of the weld, encapsulated  
 237 and polished for Marble solution etching, Figure 5. The geometry of the weld beads is revealed by  
 238 this chemical attack in order to analyze their cross shape and compare them with the results provided  
 239 by the model. Moreover, secondary dendrite arms spacing (SDAS) in the samples is measured for the  
 240 cases where the minimum and maximum powers are applied (350 W and 500 W, respectively).  
 241 Finally, the measured SDAS is compared with the values predicted by the numerical model.  
 242



243  
 244 **Figure 5.** Upper view (left), cross section (center) and detail of the microstructure (right) of the Test 6.  
 245

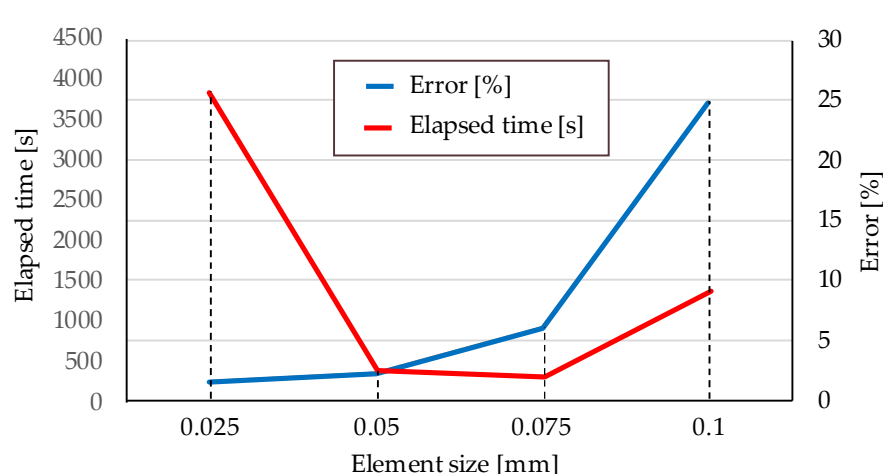
246 **Table 3.** Process parameters for the different tests

Test number	Laser power (W)	Feed rate ( $\text{mm}\cdot\text{s}^{-1}$ )	Peripheral speed ( $\text{mm}\cdot\text{s}^{-1}$ )	Argon feed ( $\text{l}\cdot\text{min}^{-1}$ )	Seam length (mm)	Wobble diameter (mm)
1	350	3	84.8	24	30	0.9
2	350	5	141.4	24	30	0.9
3	400	3	84.8	24	30	0.9
4	400	5	141.4	24	30	0.9
5	450	3	84.8	24	30	0.9
6	450	5	141.4	24	30	0.9
7	500	3	84.8	24	30	0.9
8	500	5	141.4	24	30	0.9

## 247 3.1. Model parameters

248 The modeled cross section has an 8x4 mm size in the X and Y directions, respectively. Notice  
 249 that in  $x=0$  a symmetry boundary condition is considered (see Figure 2). The distant face in this  
 250 direction must be placed at a far enough from the laser beam source in order to avoid any  
 251 disturbances in the generated thermal field, but without putting far away in order to avoid,  
 252 computational cost increased in vain. On the other hand, in the Y direction, a 1 mm layer of air is  
 253 considered below and above the sheets to be welded, which is enough for allowing the free  
 254 movement of the air-filled elements.

255 Defining an appropriate element size is critical when achieving a good relation between  
 256 accuracy and computational cost. After testing with 0.1, 0.075, 0.05, 0.025 mm size elements and  
 257 evaluating the obtained accuracy and the elapsed time required for the simulation, it is considered  
 258 that a 0.05 mm element size is the optimum value. As it can be observed in Figure 6, after simulating  
 259 the Test 4 with different element sizes, an error below 5% is obtained with a 0.05mm element size  
 260 when the depth of the weld bead is measured, together with an elapsed time of 392.95 s.  
 261



262  
 263 **Figure 6.** Variation of the elapsed time required for running the simulation and the obtained error  
 264 compared with the experimentally measured depth of the weld bead as the element size varies for the case of  
 265 the Test 4.  
 266

267 Besides, obtained results depend on the time increment used in simulation. For the present  
 268 validation, a 0.001s time step is used. A higher time step means that fewer steps are required for  
 269 sweeping the desired time interval, whereas a smaller time step means the opposite. However, higher  
 270 time step results in higher variations of the pressure and velocity fields, and consequently, the  
 271 number of required iterations before achieving the desired accuracy is also increased. In addition,  
 272 instabilities may appear, resulting in the necessity of lowering the under-relaxation factors used in  
 273 the SIMPLE algorithm (0.8 and 0.5 for the pressure and velocities calculation, respectively).

274 The cooling stage has direct impact in the final shape of the melt pool [29], as well as the  
 275 developed microstructure [30]. Therefore, an extra time is simulated after the laser passes over the  
 276 modeled cross section is in order to analyze the cooling stage and the solidification of the material. A  
 277 total simulation times of 1.0 s and 0.6 s are defined for the tests where  $3 \text{ mm}\cdot\text{s}^{-1}$  and  $5 \text{ mm}\cdot\text{s}^{-1}$  feed rates  
 278 are used, respectively.

## 279 3.2. Materials

280 Inconel 718 sheets with a 2 mm thickness are used for LBW tests. This value is similar to the  
 281 thickness of the sheets used in the aerospace gas turbines.  
 282  
 283  
 284

285

**Table 4.** Inconel 718 composition (% w.t.) ([31])

Al	B	C	Co	Cr	Cu	Fe	Mn	Mo	Ni
0.55	0.004	0.054	0.28	18.60	0.05	18.60	0.24	3.03	52.40
P	S	Si	Ti	Nb	Ta	Bi	Pb	Ag	
<0.005	<0.002	0.06	0.98	4.89	<0.05	<0.00003	<0.0005	<0.0002	

286

287

**Table 5.** Properties of Inconel 718 (Average thermo-physical properties of Inconel 718 [32])

Definition	Unit	Value
Melting range ( $T_m$ )	K	1533–1609
Density ( $\rho$ )	$\text{Kg}\cdot\text{m}^{-3}$	8190
Specific heat ( $c$ )	$\text{J}\cdot\text{kg}^{-1}\cdot\text{K}^{-1}$	435
Conductivity ( $k$ )	$\text{W}\cdot\text{m}^{-1}\cdot\text{K}^{-1}$	8.9
Latent heat fusion ( $S_L$ )	$\text{J}\cdot\text{kg}^{-1}$	$210\times 10^3$
Density ( $\rho_L$ ) (liquid phase)	$\text{Kg}\cdot\text{m}^{-3}$	7400
Specific heat ( $c_L$ ) (liquid phase)	$\text{J}\cdot\text{kg}^{-1}\cdot\text{K}^{-1}$	720
Conductivity ( $k_L$ ) (liquid phase)	$\text{W}\cdot\text{m}^{-1}\cdot\text{K}^{-1}$	29.6

288

289

290

291

292

293

294

295

296

297

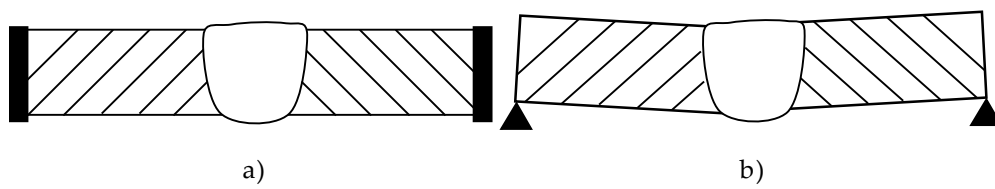
### 3.3. Experimental setup

298

299

300

Test parts are clamped to avoid distortions caused by thermal expansion or contraction during the melting and solidification process, Figure 7, which could cause misalignment in the weld zone.



301

302

303

**Figure 7.** Test parts placing examples: Properly clamped (a) and simply supported (b)

304

305

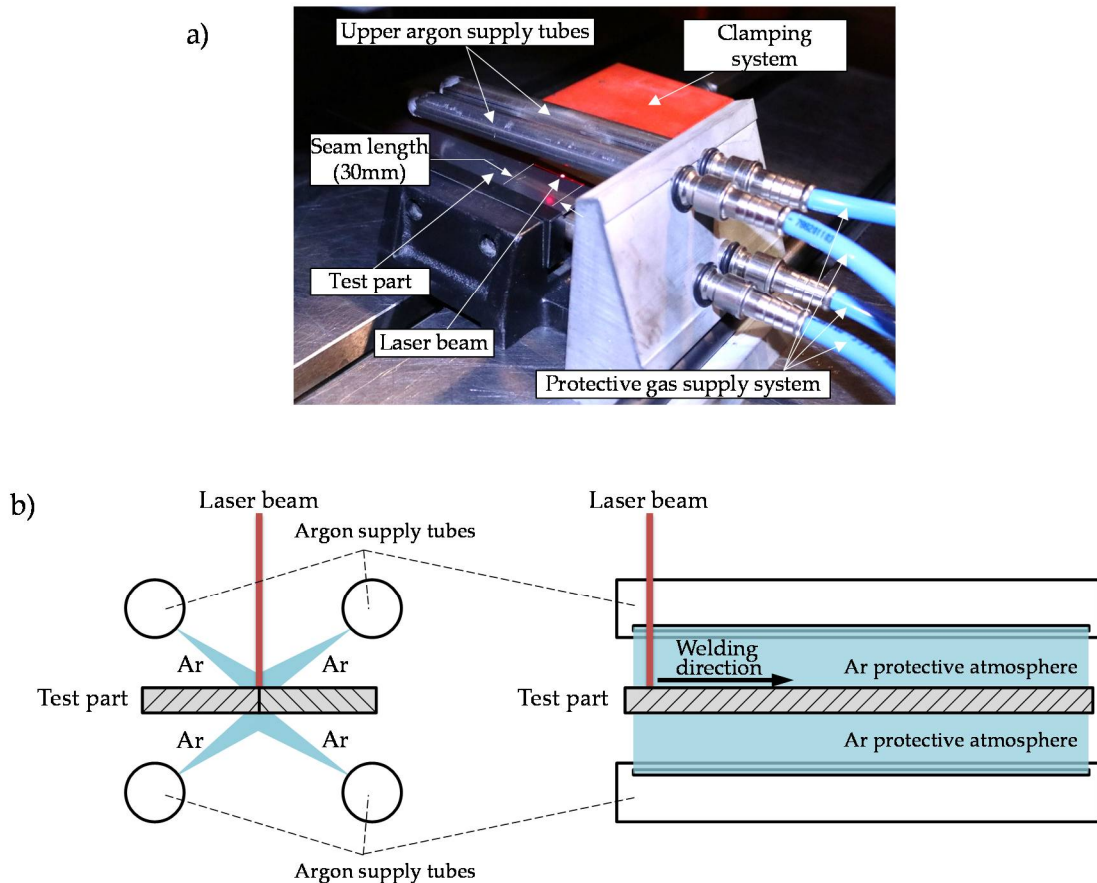
306

307

308

309

The welding process is performed with an argon 2X protective atmosphere (99.995% of argon purity). The argon gas is inserted through four slots situated in four cylindrical tubes, two pointing to the welding upper surface and the two others to the bottom one, which ensures a homogenous supply all along the seam path (see Figure 8). The argon supply is of  $24 \text{ l}\cdot\text{min}^{-1}$  ( $6 \text{ l}\cdot\text{min}^{-1}$  through each  $80 \text{ mm} \times 2 \text{ mm}$  rectangular slot).

310  
311  
312

**Figure 8.** a) Experimental setup for ensuring the protective atmosphere during the LBW tests;  
b) Frontal and lateral schematic views.

#### 313 4. Results

314 The developed model calculates the temperature field at different time steps as the laser beam  
315 passes over the modeled section. As a consequence of the temperature gradients generated within  
316 the molten material, Marangoni forces are generated and lead to creation of convection currents, see  
317 Figure 9. The size of the melt pool is increased as the interaction time increases and can reach a  
318 situation in which the whole thickness of the Inconel 718 sheet is melted (this situation occurs at a  
319  $t=0.28$  s instant in Test 5, 450 W laser power and  $v_t=3$  mm·s $^{-1}$ ) and molten material starts to drop due  
320 to gravity forces. After the laser beam passes by the modeled cross section and there is no external  
321 heat input, the material solidifies, resulting in the final shape of the generated weld bead. This final  
322 shape together with the area melted during the whole process is compared with the experimental  
323 results when validating the model.

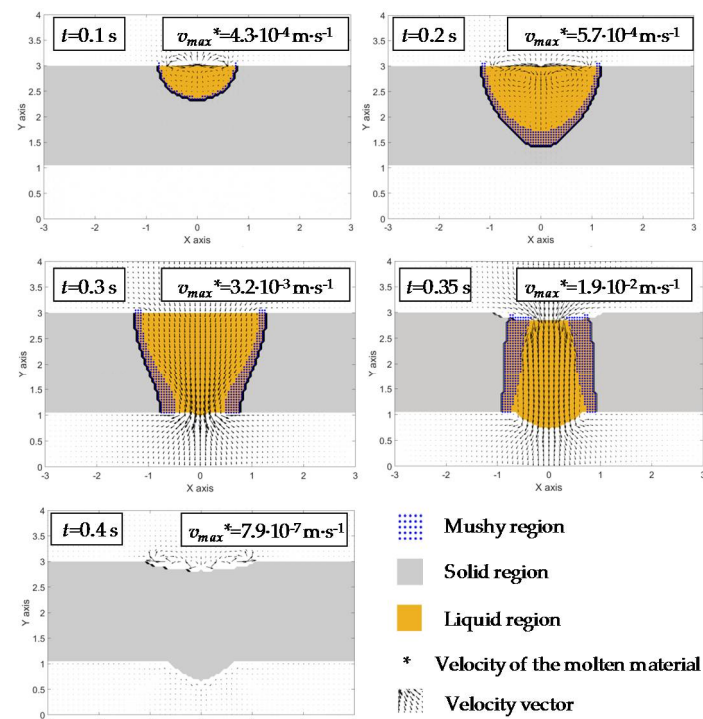
324  
325

Figure 9. Evolution of the welding section and material velocity in Test 5 as the laser beam passes.

## 326 4.1. Analysis of the geometry of the weld beads

327 In order to validate the developed model, the weld beads from the different tests are measured  
 328 taking into account the following features (see Figure 10): penetration depth (named with the letter  
 329 D), weld bead width (named with the letter W) and height both in the crown and the root (named  
 330 with the letters A and R, respectively). Due to the movement of the molten material during the  
 331 welding process, the surface tension generates fillets or groovy shapes at the weld crown. The molten  
 332 material also may stick out at the root when the penetration is complete, forming saggings or  
 333 saggings beyond the lower surface. The established sign criterion is positive (+) for fillets and saggings and  
 334 negative (-) for grooves.

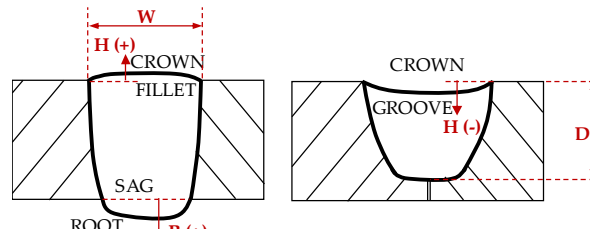
335  
336  
337  
338

Figure 10. Scheme of the different cross sections of the weld bead.

Table 6. Geometrical validation of the model (width and depth).

Test number	Crown Width (W)			Depth (D)		
	Experimental (mm)	Model (mm)	Error (%)	Experimental (mm)	Model (mm)	Error (%)
1	2.16	2.30	6.38	2.00	2.00	0.00
2	1.98	1.80	9.09	1.09	1.05	3.93
3	2.42	2.50	3.52	2.00	2.00	0.00
4	2.07	2.00	3.19	1.30	1.33	2.47
5	2.56	2.60	1.76	2.00	2.00	0.00
6	2.40	2.20	8.37	1.72	1.75	1.74
7	2.82	2.62	7.13	2.00	2.00	0.00
8	2.61	2.35	9.82	2.00	2.00	0.00

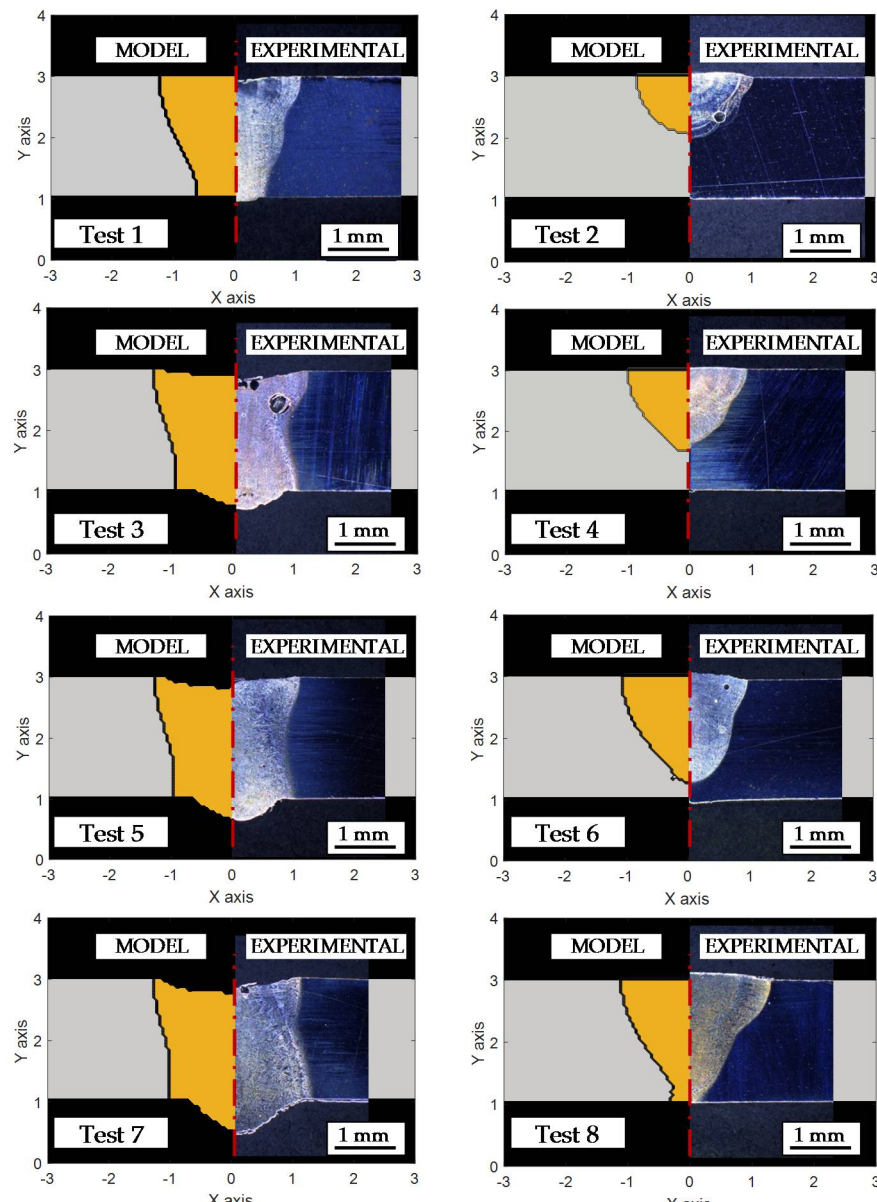
339

**Table 7.** Geometrical validation of the model (fillet-groove and sag)

Test number	Crown Height (H)			Root Height (R)		
	Experimental (mm)	Model (mm)	Error (mm)	Experimental (mm)	Model (mm)	Error (mm)
1	-0.11	0.00	0.11	0.07	0.00	0.07
2	0.09	0.00	0.09	0.00	0.00	0.00
3	-0.16	-0.10	0.06	0.31	0.25	0.06
4	0.04	0.00	0.04	0.00	0.00	0.00
5	-0.20	-0.20	0.00	0.43	0.45	0.02
6	0.16	0.00	0.16	0.00	0.00	0.00
7	-0.16	-0.25	0.09	0.58	0.50	0.08
8	0.10	0.00	0.10	0.07	0.00	0.07

340

341 The numeric model shows an error below 4% regarding to the weld bead penetration depth and  
 342 a less than 10% error for the crown width, Table 6. For both the crown and root height prediction, the  
 343 model shows an error smaller than 0.2 mm, Table 7. In Figure 11 a comparison between the modeled  
 344 and the measured cross sections is shown for the Tests 1-8.

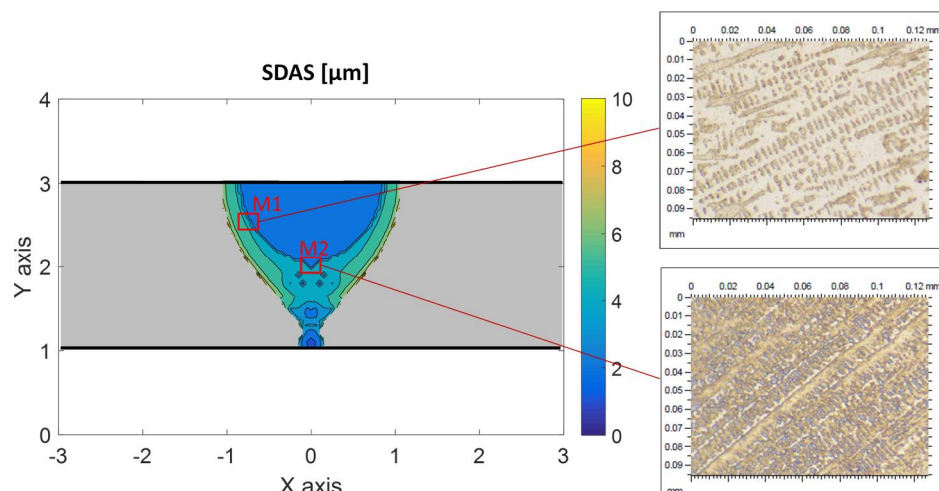
**Figure 11.** Comparison between the modeled and the analyzed cross sections.

345

346

## 347 4.2. Microstructure validation

348 The microstructure is studied for the Tests 1, 2, 7 and 8 and in each case, as detailed in Figure 12,  
 349 two different areas are studied for validating the model prediction of the SDAS value. The first one  
 350 (M1) is located near the boundary between the weld bead and the HAZ and it is the first area where  
 351 the material solidifies after its melting, whereas the second one (M2) is placed in the center of the  
 352 bead.



353  
 354 **Figure 12.** Secondary dendrite arm spacing (SDAS) of Test 8 together with the experimental  
 355 microstructure details in regions M1 and M2.

356 The analysis of the experimental tests is carried out by a Leica DCM 3D microscopy with 100X  
 357 magnification. For each study zone, the SDAS measurements are performed and the average value is  
 358 calculated, which is compared with the results given by the numerical model, see Table 8. The  
 359 maximum error between the predicted SDAS values and the measured ones is below 1.5 microns,  
 360 which means that there is a good agreement between the model and the experimental process. Also,  
 361 since the microstructure depends on the cooling rate, which depends on the variation of the thermal  
 362 field, so, it can be concluded that the model predicts the temperature field accurately during the LBW  
 363 process.

364 **Table 8.** Microstructure validation of the model.

Test number	Area M1			Area M2		
	Model (μm)	Experimental (μm)	Error (μm)	Model (μm)	Experimental (μm)	Error (μm)
1	2.71	3.19	-0.48	2.77	3.70	-0.93
2	2.21	3.05	-0.84	2.04	2.58	-0.54
7	2.31	3.78	-1.47	2.82	4.25	-1.43
8	2.08	3.54	-1.46	1.83	2.63	-0.80

## 365 5. Conclusions

366 In the present work, a numerical model for predicting the weld bead in the LBW process is  
 367 developed and validated under different process parameters. According to the obtained results, the  
 368 following conclusions can be drawn:

369 (1) The developed model represents accurately the weld beads generated under different process  
 370 parameters. In all cases, the maximum error is lower than the 10% regarding the weld bead  
 371 width and depth, which ensures a high agreement between the model and the tests.

372 (2) The developed tool is valid for modeling not only the melt pool dynamics, but also the drop of  
 373 the molten material once the laser beam melts the whole thickness of the Inconel 718 sheets.  
 374 An error below 0.2 mm is detected between the model and the experimental results in the  
 375 crown and root heights of the weld bead. However, the model resulted incapable of predicting  
 376 the height of the fillet if the bead is not complete.

377 (3) After comparing the microstructure measured in the experimental tests and the values given  
378 by the model, it is concluded that the model gives the SDAS with an error below 1.5 microns.  
379 The two different areas that are analyzed (M1 and M2) show that the SDAS in the test tubes is  
380 slightly higher than the value given by the model. Hence, it is concluded that the predicted  
381 cooling rate is also somewhat higher than the real one. This can be originated by the symmetry  
382 assumption or the two-dimensional solving of the melt pool dynamics, whereas the physical  
383 problem is three-dimensional.

384 Therefore, the proposed model results to be appropriate for modeling the LBW process and can  
385 be used as a predictive tool for simulating weld beads before carrying out real tests. Therefore, it has  
386 a direct application on aerospace industry and specifically in Inconel 718 welds.

387 **Author Contributions:** Iñigo Hernando conceived, designed and performed the experiments; Iñigo Hernando  
388 and Jon Iñaki Arrizubieta developed the numerical model; Eneko Ukar and Aitzol Lamikiz analyzed the data.  
389 Aitzol Lamikiz reviewed previous works related with the subject. Iñigo Hernando and Jon Iñaki Arrizubieta  
390 wrote the paper.

391 **Funding:** This research received no external funding.

392 **Acknowledgments:** Thanks are addressed to H2020-FoF13-2016 PARADDISE project (contract number 723440).  
393 Special thanks are addressed to the University of the Basque Country (UPV-EHU) for the funding support  
394 received from the contracting call for the training of research staff in UPV-EHU 2015.

395 **Conflicts of Interest:** The authors declare no conflict of interest.

## 396 References

- 397 1. Liu, S.; Mi, G.; Yan, F.; Wang, C.; Jiang, P.; Correlation of high power laser welding parameters with real  
398 weld geometry and microstructure. *Optics & Laser Technology*, **2017**, *94*, 59-67.  
399 DOI:10.1016/j.optlastec.2017.03.004
- 400 2. D’Ostuni, S.; Leo, P.; Casalino, G. FEM Simulation of Dissimilar Aluminum Titanium Fiber Laser Welding  
401 Using 2D and 3D Gaussian Heat Sources. *Metals*, **2017**, *7*, 307. DOI:10.3390/met7080307
- 402 3. Kazemi, K.; Goldak, J.A. Numerical simulation of laser full penetration welding. *Computational Materials  
403 Science*, **2009**, *44*, 841-849. DOI:10.1016/j.commatsci.2008.01.002
- 404 4. Venkatesan, K.; Ramanujam, R.; Kuppan, P. Parametric modeling and optimization of laser scanning  
405 parameters during laser assisted machining of Inconel 718. *Optics & Laser Technology*, **2016**, *78*, 10-18.  
406 DOI:10.1016/j.optlastec.2015.09.021
- 407 5. Anderson, M.; Patwa, R.; Shin, Y.C. Laser-assisted machining of Inconel 718 with an economic  
408 analysis. *International Journal of Machine Tools and Manufacture*, **2006**, *46*, 1879-1891.  
409 DOI:10.1016/j.ijmachtools.2005.11.005
- 410 6. Ram, G.D.J.; Reddy, A.V.; Rao, K.P.; Reddy, G.M.; Sundar, J.K.S. Microstructure and tensile properties of  
411 Inconel 718 pulsed Nd-YAG laser welds. *Journal of Materials Processing Technology*, **2005**, *167*, 73-82.  
412 DOI:10.1016/j.jmatprotec.2004.09.081
- 413 7. Steen, W.M.; Mazumder, J. *Laser material processing*, 4<sup>th</sup> ed.; Springer: London, England, 2010. ISBN 978-1-  
414 84996-061-8
- 415 8. Davis, J.R. *ASM specialty handbook: nickel, cobalt, and their alloys*. ASM International: Ohio, USA, 2000.
- 416 9. Dowden, J.M. The mathematics of thermal modeling: an introduction to the theory of laser material  
417 processing, Chapman & Hall/CRC: Boca Raton, USA, 2001. ISBN 978-1-58488-230-5
- 418 10. Mazumder, J. Laser welding. In *Laser materials processing*, 1st ed.; Bass, M.; Elsevier: New York, USA, 1983;  
419 Volume 3, pp. 120-200. ISBN 0-444-86396-6
- 420 11. Brown, M.S; Arnold, C.B. Fundamentals of Laser-Material Interaction and Application to Multiscale  
421 Surface Modification. In *Laser precision microfabrication*, 1st ed.; Sugioka, K.; Meunier, M.; Piqué,  
422 A.; Springer: London, England. 2010. ISBN 978-3-642-10522-7
- 423 12. Mills, K. C., Keene, B.J.; Brooks, R.F.; Shirali, A. Marangoni effects in welding. *Philosophical Transactions of  
424 the Royal Society a Mathematical Physical and Engineering Sciences*, **1998**, *356*, 911-926.  
425 DOI: 10.1098/rsta.1998.0196
- 426 13. Swift-Hook, D. T.; Gick, A.E.F. Penetration welding with lasers. *Welding journal*, **1973**, *52*, 492-499.

427 14. Klemens, P. G. Heat balance and flow conditions for electron beam and laser welding. *Journal of Applied*  
428 *physics*, **1976**, *47*, 2165-2174. DOI:10.1063/1.322866

429 15. Goldak, J.; Chakravarti, A.; Bibby, M. A new finite element model for welding heat sources. *Metallurgical*  
430 *transactions B*, **1984**, *15*, no 2, p. 299-305. DOI: 10.1007/BF02667333

431 16. Bonollo, F.; Tiziani, A.; Zambon, A. Model for CO<sub>2</sub> laser welding of stainless steel, titanium, and nickel: *parametric study. Materials Science and Technology*, **1993**, *9*, 1137-1144. DOI:10.1179/mst.1993.9.12.1137

432 17. Kaplan, A. A model of deep penetration laser welding based on calculation of the keyhole profile. *Journal*  
433 *of Physics D: Applied Physics*, **1994**, *27*, 1805-1814. DOI:10.1088/0022-3727/27/9/002

435 18. Ducharme, R.; Williams, K.; Kapadia, P.; Dowden, J.; Steen, B.; Glowacki, M.. The laser welding of thin  
436 metal sheets: an integrated keyhole and weld pool model with supporting experiments. *Journal of physics*  
437 *D: Applied physics*, **1994**, *27*, 1619-1627. DOI:10.1088/0022-3727/27/8/006

438 19. Sudnik, W.; Radaj, D.; Breitschwerdt, S.; Erofeew, W. Numerical simulation of weld pool geometry in laser  
439 beam welding. *Journal of Physics D: Applied Physics*, **2000**, *33*, 662-671. DOI:10.1088/0022-3727/33/6/312

440 20. Tsirkas, S.A.; Papanikos, P.; Kermanidis, Th. Numerical simulation of the laser welding process in butt-  
441 joint specimens. *Journal of materials processing technology*, **2003**, *134*, 59-69.  
442 DOI:10.1016/S0924-0136(02)00921-4

443 21. Gery, D.; Long, H.; Maropoulos, P. Effects of welding speed, energy input and heat source distribution on  
444 temperature variations in butt joint welding. *Journal of materials processing technology*, **2005**, *167*, 393-401.  
445 DOI:10.1016/j.jmatprotec.2005.06.018

446 22. Zhao, H.; Niu, W.; Zhang, B.; Lei, Y.; Kodama, M.; Ishide, T. Modelling of keyhole dynamics and porosity  
447 formation considering the adaptive keyhole shape and three-phase coupling during deep-penetration laser  
448 welding. *Journal of Physics D: Applied Physics*, **2011**, *44*, 485302. DOI:10.1088/0022-3727/44/48/485302

449 23. Kubiak, M; Piekarska, W.; Saternus, Z.; Domanski, T. Numerical prediction of fusion zone and heat affected  
450 zone in hybrid Yb: YAG laser+ GMAW welding process with experimental verification. *Procedia*  
451 *Engineering*, **2016**, *136*, 88-94. DOI: 10.1016/j.proeng.2016.01.179

452 24. Zhang, L.J.; Zhang, J.X.; Gumennyuk, A.; Rethmeier, M.; Na, S.J. Numerical simulation of full penetration  
453 laser welding of thick steel plate with high power high brightness laser. *Journal of materials processing*  
454 *technology*, **2014**, *214*, 1710-1720. DOI:10.1016/j.jmatprotec.2014.03.016

455 25. Patankar, S.V. *Numerical heat transfer and fluid flow*, 1st ed.; McGraw-Hill, 1980. ISBN-13:978-0891165224

456 26. Voller, V.R.; Prakash, C. A fixed grid numerical modelling methodology for convection-diffusion mushy  
457 region phase-change problems. *International Journal of Heat and Mass Transfer*, **1987**, *30*, 1709-1719.  
458 DOI:10.1016/0017-9310(87)90317-6

459 27. Patel, A.D.; Murty, Y.V. Effect of cooling rate on microstructural development in alloy 718. International  
460 symposium; 5th, Superalloys; Superalloys 718, 625, 706 and various derivatives, Warrendale (USA), 2001,  
461 123-132.

462 28. Antonsson, T.; Fredriksson, H. The effect of cooling rate on the solidification of Inconel 718. *Metallurgical*  
463 *and Materials Transactions B*, **2005**, *36*, 85-96. DOI:10.1007/s11663-005-0009-0

464 29. Saldi, Z. S.; Kidess, A.; Kenjeres, S.; Zhao, C.; Richardson, I.M., Kleijin, C.R. Effect of enhanced heat and  
465 mass transport and flow reversal during cool down on weld pool shapes in laser spot welding of  
466 steel. *International Journal of Heat and Mass Transfer*, **2013**, *66*, 879-888.  
467 DOI:10.1016/j.ijheatmasstransfer.2013.07.085

468 30. Zhang, Y. N.; Cao, X.; Wanjara, P. Microstructure and hardness of fiber laser deposited Inconel 718 using  
469 filler wire. *The International Journal of Advanced Manufacturing Technology*, **2013**, *69*, 2569-2581.  
470 DOI:10.1007/s00170-013-5171-y

471 31. Haynes International. Material Sales order 810002010-0; Customer reference 20PPO009192; Report No.  
472 20151117074

473 32. Mills, K.C. *Recommended values of thermophysical properties for selected commercial alloys*, 1st ed.; Woodhead  
474 Publishing: Cambridge, England, 2002; pp. 181-190. ISBN 1 85573 569 5